Gas adsorption on quasicrystalline surfaces

2008 J. Phys.: Condens. Matter 20 314007

(http://iopscience.iop.org/0953-8984/20/31/314007)

J. Phys.: Condens. Matter **20** (2008) 314007 (10pp) doi:10.1088/0953-8984/20/31/314007

Gas adsorption on quasicrystalline surfaces

R D Diehl[1], W Setyawan[2] and S Curtarolo[2]

[1] Department of Physics, Penn State University, University Park, PA 16802, USA
[2] Department of Mechanical Engineering and Materials Science, Duke University, Durham, NC 27708, USA

Received 7 April 2008
Published 11 July 2008
Online at stacks.iop.org/JPhysCM/20/314007

Abstract

The low-friction properties of quasicrystal surfaces suggest their use as coatings on moving machine parts, including those in internal combustion engines. In such applications, additional lubricants are typically used. Since the low-friction properties of quasicrystals are thought to depend on their aperiodic structures, the interactions of lubricants on quasicrystalline surfaces may have an impact on their frictional properties. In this paper, we address the fundamental issues that affect the growth and structural properties of gases on a quasicrystal surface. Studies of the adsorption and growth of rare gases on quasicrystal surfaces are reviewed, and new results are presented for the modeling and simulation of hydrocarbons on quasicrystal surfaces. The calculated interaction parameters are presented for methane adsorption on ten-fold Al–Ni–Co. Methane is found to form aperiodically ordered structures, consistent with the rules established earlier for rare gases on Al–Ni–Co.

(Some figures in this article are in colour only in the electronic version)

1. Introduction

The low-friction properties of quasicrystals in ambient conditions coupled with their high hardness and oxidation resistance led to the development of applications of quasicrystal coatings, for instance on machine parts, cutting blades, and non-stick frying pans [1]. In such practical applications, hydrocarbons are commonly used as a lubricant. Superlubricity is the name given to the phenomenon in which two parallel single crystal surfaces slide over each other with vanishingly small friction because their structures are incommensurate. This phenomenon was proposed in the early 1990s and experimental evidence for this effect has been seen in studies of mica sliding on mica [2], W(110) on Si(100) [3], Ni(100) on Ni(100) [4], and graphite on graphite [5]. Although there are other factors in these systems, aside from incommensurability, that affect the friction, superlubricity may play a major role in the friction of quasicrystals because of their aperiodic structures. Indeed, quasicrystal surfaces were observed to have low friction not long after they were first discovered [6], but pinning down the exact origin of the low friction has been elusive [7]. Recent experiments in ultra high vacuum (UHV) have demonstrated a frictional dependence on aperiodicity for both atomically clean quasicrystals and quasicrystals with chemisorbed films in UHV, although this was attributed mainly to weaker phononic coupling with the aperiodic surfaces [8–12]. In coating applications, whatever the origin of the lower friction, some additional lubricant would still be needed to counter the frictional contributions due to grain boundaries, asperities and other defects in the surfaces of the moving parts. If superlubricity plays a role, then the lubricant in such a situation must not remove or reduce that effect. Similarly, if reduced phonon coupling is important, then this must be maintained with the lubricant. Therefore it is desirable to have a good understanding of how gases, hydrocarbons in particular, interact with quasicrystal surfaces.

Although the growth of films on quasicrystalline surfaces has been studied for some years [7, 13–17], very little is known about the interaction of hydrocarbons, their structures and growth on alloy or quasicrystalline surfaces. Some earlier experiments suggest that certain hydrocarbons, such as formic acid, HCOOH, dissociate on the five-fold surface of Al–Pd–Mn, whereas it does not on the ten-fold surface of Al–Ni–Co [18]. Benzene, C_6H_6, on the other hand, does not dissociate on Al–Pd–Mn, and apparently orders in a quasicrystalline structure [19]. Ethylene is believed to form a disordered chemisorbed monolayer on Al–Ni–Co [12].

To obtain a fundamental understanding of the interactions of hydrocarbons with quasicrystal surfaces, it is helpful to use rare gases as models that can elucidate the characteristics that

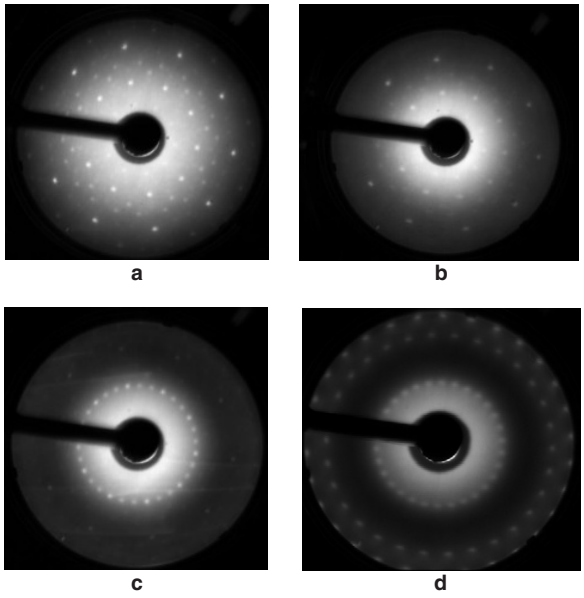

Figure 1. LEED patterns taken with a primary electron beam energy of 62 eV from (a) clean Al–Ni–Co, (b) after adsorption of one layer of Xe, (c) after adsorption of two layers of Xe, and (d) after adsorption of several layers of Xe, for a constant pressure of 3.2×10^{-7} mbar. Figure 1 in [26] (Copyright (2004) by the American Physical Society).

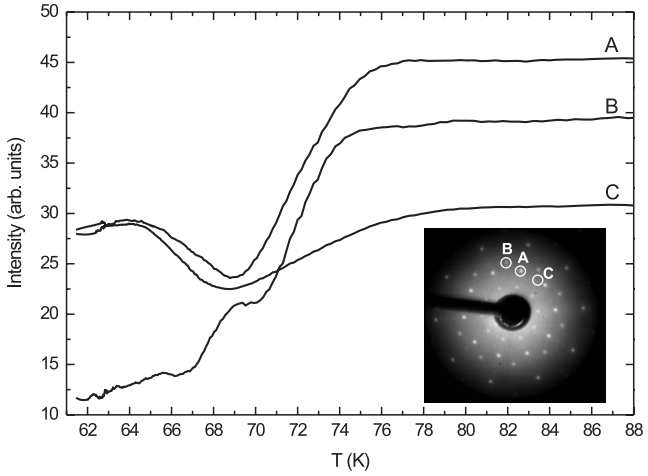

Figure 2. LEED adsorption isobar curves for Xe on Al–Ni–Co, showing the integrated intensity of three different diffraction spots at a constant pressure of 1.6×10^{-6} mbar. The inset clean surface LEED pattern (55 eV) shows the corresponding diffraction spots. A and B are substrate spots, C is solely due to the Xe overlayer. The location of substrate spot A is also the location of a Xe spot when ordering occurs, hence it decreases in intensity during monolayer adsorption but increases when the Xe orders. Spot C has no associated substrate diffraction spot, but has some initial intensity due to the low-intensity diffraction features characteristic of aperiodic structures [30]. Figure 3 in [26] (Copyright (2004) by the American Physical Society).

arise from the 'physical' parameters of the adsorption, such as relative adsorbate and substrate length scales, interaction strengths, substrate corrugation, film growth and phase transitions. In this paper, we review what is known about the structural properties of rare gases on quasicrystal surfaces and present preliminary results of a study to model hydrocarbons on quasicrystalline Al–Ni–Co.

2. Inert gases on Al–Ni–Co

2.1. Xe adsorption

A combined low-energy electron diffraction (LEED) and grand canonical Monte Carlo (GCMC) study of the adsorption of Xe on the ten-fold surface of Al–Ni–Co has provided a great deal of insight into the effects of a quasicrystalline adsorption potential on the structures and growth of these films. The basis for these studies was an LEED structural study of the clean Al–Ni–Co surface [20], which indicated that the surface of Al–Ni–Co is an unreconstructed termination of the bulk structure. A small amount of surface relaxation (<0.2 Å contraction for the top layer spacing) and buckling of the surface (displacements <0.1 Å from bulk positions) was observed. The composition of the Al–Ni–Co sample used in this study was $Al_{73}Ni_{10}Co_{17}$, which puts it in the region of the basic Co-rich phase. The structure model used in the LEED analysis was that derived from a bulk x-ray diffraction study of the Ni-rich phase [21], but it was thought that since LEED is not sensitive to the difference between Co and Ni that any differences would be minimal. A later analysis of the same experimental data used various periodic approximants for structure models, producing essentially the same result [22]. More recently, the W-approximant, having a larger unit cell, and which is thought to be closely related to the structure of d-Al–Ni–Co, was used as a structure model, again with a very similar result [23]. This structure is also consistent with an *ab initio* study of the Ni-rich surface of the W-approximant [24], which was based on a variant of the bulk structure of the Co-rich W-approximant determined by x-ray diffraction [25].

This surface was used as the substrate in a series of LEED experiments to characterize the structure, growth, and thermodynamics of Xe adsorption on an aperiodic substrate [26]. Representative LEED patterns obtained during Xe adsorption are shown in figure 1, and equilibrium LEED isobars are shown in figure 2. The main findings of that study were as follows.

(1) The Xe grows in a layer-by-layer mode at temperatures between 60 and 80 K.
(2) The structure of the Xe at submonolayer coverages has the same symmetry as the substrate and most likely adopts a 'commensurate' quasicrystalline structure.
(3) At the onset of second-layer adsorption, a hexagonal overlayer forms, containing five rotational domains and aligned along the symmetry directions of the substrate.
(4) For higher coverages, the structure of the film is consistent with face-centered cubic Xe(111).
(5) The heat of adsorption for the first Xe layer is 250 ± 10 meV, comparable to Xe on other metal substrates.

While, in principle, LEED could be used to determine the locations of the Xe atoms in the monolayer structure,

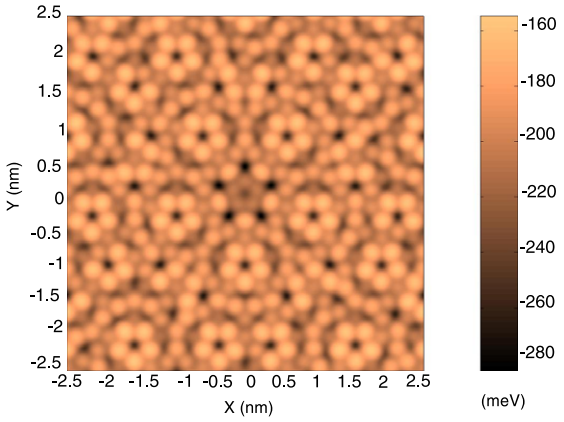

Figure 3. Minimum potential energy surface for Xe on a 5.12×5.12 nm^2 section of the Al–Ni–Co quasicrystal. The scale at the right shows the energy scale, which ranges from -280 to -160 meV. The energy contours generally follow the substrate atoms, with tops being less favorable and hollows being more favorable. Figure 1 in [31] (Copyright (2005) by the American Physical Society).

the fact that Xe is a relatively weak scatterer (owing mainly to its large perpendicular vibration amplitude [27]) hindered further analysis of this structure. Attempts to image this structure using scanning tunneling microscopy (STM) also failed, apparently because tunneling cannot be established from Xe on the weakly conducting Al–Ni–Co. Therefore, to gain a deeper understanding of these and other aspects of the Xe adsorption, grand canonical Monte Carlo simulations were employed.

The Xe-quasicrystal interaction potential was modeled by using Lennard-Jones potentials between the Xe and the individual substrate atoms and between Xe atoms [28]. Using this potential, thermodynamic calculations were carried out for the low coverage regime. The heat of adsorption was found to agree with the experimental value. Interestingly, it was found that the effect of the substrate corrugation, which is much larger than is typical for low-index surfaces of metal surfaces (120 meV versus ∼30 meV [29]), is to enhance the Xe–Xe attraction on the surface.

To obtain further insight, this potential was applied to grand canonical Monte Carlo simulations [31–33]. In these simulations, the main results are obtained from simulating equilibrium adsorption isotherms (figure 4(a)). These are comparable to the isobars performed in the LEED experiments, but the simulations can probe a much larger region of the pressure–temperature phase diagram. The main findings of this study were as follows.

(1) Xe grows layer-by-layer for at least five layers before bulk condensation at 77 K. There is complete wetting above the 3D triple point of Xe, and no sign of drying behavior whatsoever [47, 48].
(2) Xe grows initially in an epitaxial quasicrystalline five-fold structure, with a first-order phase transition to a hexagonal structure at a coverage somewhat below the onset of second-layer adsorption.
(3) Entropic pentagonal defects in the hexagonal structure mediate the boundaries between the five different rotational domains.

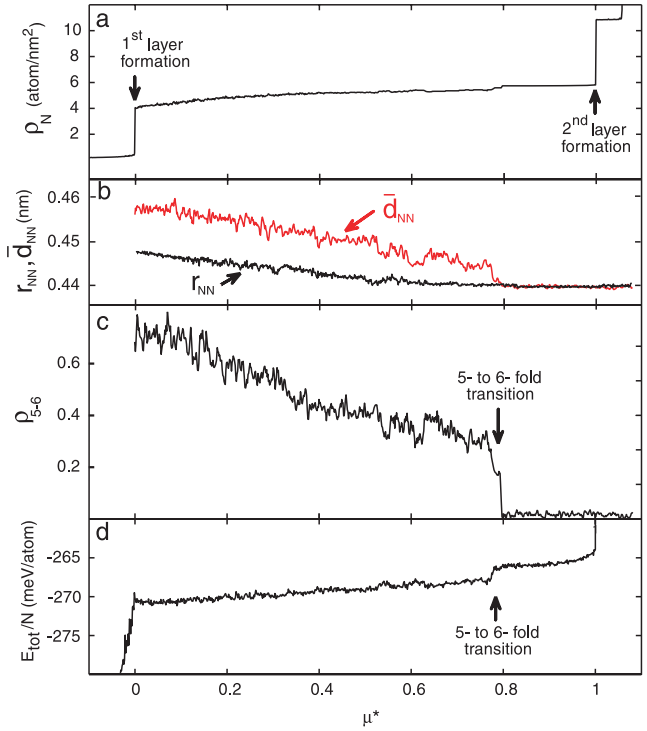

Figure 4. (a) Adsorption isotherm ρ_N versus the reduced chemical potential μ^* at $T = 77$ K. The reduced chemical potential is a fractional chemical potential defined to be 0 at the onset of first-layer adsorption and 1 at the onset of second-layer adsorption. (b) Nearest-neighbor distance defined from the pair correlation function r_{NN} (black line) and average spacing between neighbors at equilibrium, d_{NN} (red line). (c) Order parameter ρ_{5-6} (probability of five-fold defects, defined by the ratio of the number of atoms having 2D coordination number 5 to sum of the number of atoms having the 2D coordination numbers 5 and 6) versus the reduced chemical potential at $T = 77$ K, (d) total energy per adatom at $T = 77$ K. The discontinuity near $\mu^* = 0.8$ indicates a latent heat of transition. Figure 1 in [33] (Copyright (2006) by the American Physical Society).

(4) The isosteric heat of adsorption of the first Xe layer is 270 meV, compared to 250 meV found in the experiment.

The good agreement between the simulations and the experiment, exemplified by the correspondences found in film structure and growth and the first-layer heat of adsorption, gives confidence that Lennard-Jones potentials can be used for Xe adsorption on quasicrystal surfaces, even though generally they are not very good for Xe on metal surfaces [34] mainly because they do not include the static polarization effects induced in the substrate by the Xe. This correspondence gives confidence that the simulations are accurately describing the experimental situation, which is important for extending the studies beyond the experimental studies. In these simulations, it was possible to examine the structures formed by the Xe on a microscopic scale. Indeed, at the lower coverages, the Xe was found to occupy a quasicrystalline array of sites that corresponds to the points of highest adsorption energy (darkest features in figure 3). At coverages near monolayer completion, the first-layer structure has overall six-fold symmetry, with five different rotational domains, consistent with the experiment.

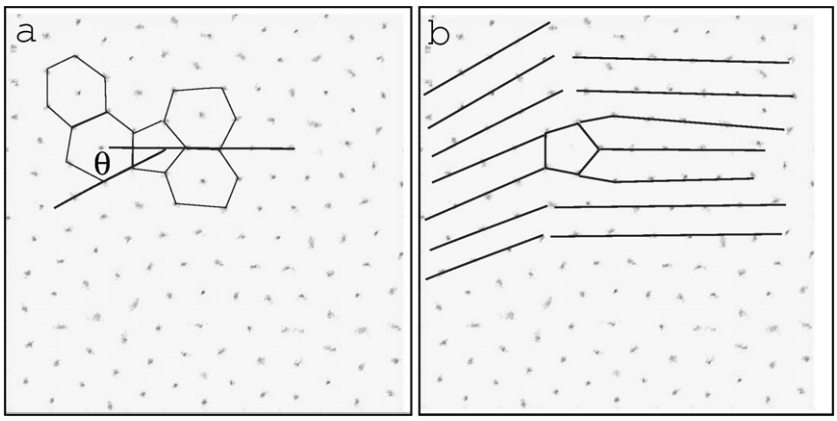

Figure 5. (a) Surface density variation for the monolayer hexagonal structure of Xe, showing that the hexagonal lattice rotates by 36° due to the presence of a pentagonal defect. (b) The same density plot showing the presence of a dislocation at the five-fold defect. Figure 4 in [32].

While such alignment with the substrate directions is common for rare gas adsorption on metals [35], it is usually a result of nucleation at the defect steps on the surface, which would be expected to run mainly along the five high-symmetry directions on this surface. Thus, at the very least, the rotational domain size is limited by the terrace size. However, examinations of the Xe density plots indicate that intrinsic pentagonal defects within the hexagonal structure mediate the formation of domain walls between differently rotated domains, as shown in figure 5 [32]. These pentagonal defects are observed to be entropic in nature [33], i.e. their density increases with temperature, and thus the average rotational domain size decreases with T. Therefore, even on a perfect substrate, the different rotational domains will be present at any finite temperature.

Perhaps the most interesting aspect of this adsorption system is the transition from the 'commensurate' five-fold structure at submonolayer coverages to the 'incommensurate' six-fold structure at somewhat higher coverages. Clearly, the commensurate five-fold structure is stabilized by the substrate corrugation. In the experimental paper, it was postulated that the hexagonal ordering is also stabilized by the substrate, due to a coincidence of the natural Xe–Xe row spacing and a characteristic distance between the quasicrystal 'rows' [26]. A detailed study of this transition was carried out using the GCMC simulations. By calculating both an order parameter of the 'commensurate' structure and the total energy of the film, the transition was found to be discontinuous (figure 4). A study of the location of the transition in the isotherms indicated that the reduced chemical potential μ at which the transition occurs varies with the temperature of the isotherm. The transition occurred at the lowest μ^* for the range 60 K $< T <$ 100 K, and at somewhat higher μ^* at higher and lower T values. This was interpreted as a result of competition between the thermal effects overriding the corrugation at the lower T values (μ^* of the transition decreasing with T) and the additional structural freedom afforded by the promotion of atoms out of the first layer (μ^* of the transition increasing with T), decreasing the effective repulsive Xe–Xe interaction that favors six-fold coordination. The question of whether the coincidence in spacing favors the formation of the hexagonal structure was not answered in these simulations, however. To our knowledge, this is the first observation of a first-order commensurate–incommensurate transition in a monolayer. Theoretical studies indicated that highly corrugated adsorption potentials lead to first-order transitions [36], consistent with this observation. The lack of earlier observations of such a transition may be related to the fact that the formation of the well-ordered incommensurate phase in this strongly corrugated case relies on the special relationship between the natural Xe spacing and the length scale of the aperiodicity. These questions concerning this coincidental matching motivated further studies of other gases on this surface.

2.2. *Other inert gas adsorption*

Building on the insight gained from the Xe studies, further theoretical studies of other inert gases on Al–Ni–Co were performed by constructing the appropriate Lennard-Jones-based potentials. Such potentials were developed for Ne, Ar, and Kr. In addition, it was found to be beneficial to create several fictitious gases having other combinations of Lennard-Jones parameters. These gases were developed to have combinations of energy and length parameters from the 'real' rare gases, e.g. one of them had a well depth corresponding to Ne but a size corresponding to Xe, thereby acting as an 'inflated' Ne. The calculated adsorption parameters for all of these gases are given in table 1.

A comparison of isotherms calculated for Ne, Ar, Kr, and Xe is shown in figure 6. Although layer-by-layer growth is observed for all of these gases, the slopes of the plateaus differ. The reason for this is that the substrate corrugation has a more pronounced effect on the structure for the smaller gases, i.e. the smaller atoms penetrate more deeply into the pockets of the substrate potential. The density profiles of the adsorbed layers for Ne, Ar, and Kr are similar to those of Xe at the lowest coverage, i.e. the gas atoms mainly occupy the lowest potential energy sites on the surface. There are differences in the evolution of the order, however, in that the smaller gases (Ne, Ar, Kr) do not make a transition to a hexagonal structure within the monolayer regime.

Table 1. Range, average ($\langle V_{\min}\rangle$), and standard deviation (SD) of the interaction $V_{\min}(x.y)$ on the QC. Effective parameters of the gas–surface interactions (D_{gs}, σ_{gs}, D^*_{gs}, σ^*_{gs}), and, for comparison, the best-estimated well depths D^{Gr}_{gs} on graphite [37]. Table 2 in [38].

	$V_{\min}$ range (meV)	$\langle V_{\min}\rangle$ (meV)	SD (meV)	D_{gs} (meV)	σ_{gs} (nm)	D^*_{gs} (D_{gs}/ε_{gg})	σ^*_{gs} (σ_{gs}/σ_{gg})	D^{Gr}_{gs} (meV)
Ne	−71 to −33	−47.43	6.63	43.89	0.260	15.03	0.935	33
Ar	−181 to −85	−113.32	13.06	108.37	0.291	10.50	0.856	96
Kr	−225 to −111	−145.71	15.68	140.18	0.301	9.52	0.836	125
Xe	−283 to −155	−195.46	17.93	193.25	0.326	10.15	0.795	162
iNe(1)	−65 to −36	−45.11	4.08	43.89	0.326	15.03	0.795	
dXe(1)	−305 to −150	−207.55	29.18	193.25	0.260	10.15	0.935	
dXe(2)	−295 to −155	−199.40	19.33	193.25	0.316	10.15	0.810	
iXe(1)	−248 to −170	−195.31	11.21	193.25	0.396	10.15	0.720	
iXe(2)	−230 to −180	−194.25	7.77	193.25	0.458	10.15	0.679	

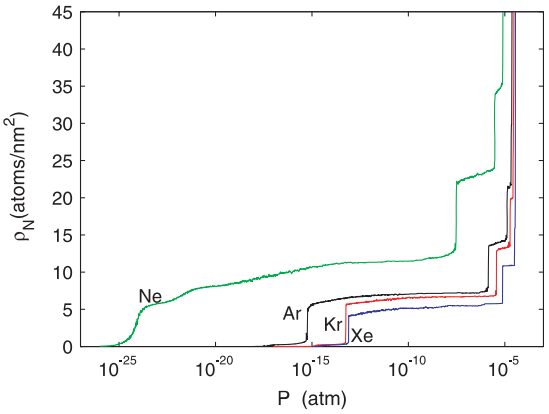

Figure 6. Calculated isotherms for Ne, Ar, Kr, and Xe on Al–Ni–Co, showing adsorbed density versus P. The T values of the isotherms are chosen so that $T = 0.35\varepsilon_{gg}$, where ε_{gg} is the Lennard-Jones gas phase interaction energy parameter. The actual T values are 11.8 K, 41.7 K, 59.6 K, and 77 K, respectively. The range of densities spanned by the first (low P) plateau is larger relative to later (high P) plateaus for each gas, and larger for the smaller gases relative to the larger gases. Figure 2 in [39].

Figure 7 shows the order parameter ρ_{5-6} for Ne, Ar, Kr, and Xe (also shown in figure 4(c) for Xe). This order parameter is defined to indicate the fraction of the atoms that have five-fold in-plane coordination. As the chemical potential μ^* increases, ρ_{5-6} decreases continuously, reaching a constant value only for Kr. At bulk condensation, the ρ_{5-6} values are still high, approximately 0.35–0.45. Data at higher T values show a similar behavior. Thus, we conclude that these gases do not undergo the commensurate–incommensurate transition observed for Xe.

In order to explore this further, fictitious gases were created, as described in table 2. These gases produced isotherms similar to those found for the 'real' gases, i.e. they are indicative of layer-by-layer growth. The calculated order parameters are more illuminating, however, as shown in figure 8. It was found that the commensurate–incommensurate transition occurs within the first-layer plateau of the isotherms for the 'inflated' Xe and Ne, but not for the 'deflated' Xe. What this reveals is that the size of the adatom determines whether the transition occurs.

Regardless of the magnitude of the holding potential, the adatom must be at least as large as Xe for the transition to occur. So indeed, it seems that the coincidence of the relative sizes of Xe and the characteristic spacing on the Al–Ni–Co surface does provide a stabilizing factor in the formation of the hexagonal structure. However, the situation is somewhat more complicated than this, because any gas larger than Xe also forms a hexagonal structure. The reason for this must be that the effect of the substrate corrugation decreases as the adatom size increases, and it may or may not be coincidental that this critical size is the average distance between 'troughs' on the quasicrystal.

3. Hydrocarbon gases on Al–Ni–Co

The pair potentials used in the rare gas studies described above are not sufficient for the computer simulation studies of hydrocarbons on quasicrystals because the adsorption interactions are more complex. In this section, we describe the method for generating appropriate potentials for hydrocarbons on quasicrystals, and preliminary results for the adsorption of methane on the same Al–Ni–Co surface that is described above.

The intermolecular (adsorbate–adsorbate) interactions are calculated as a sum of pair interactions between atoms. For methane–methane, Buckingham-type potentials are used

$$V(r) = A\exp(-Br) - C/r^6$$

with the parameters C–C ($A = 1894$ kJ mol^{-1}, $B = 2.693$ Å^{-1}, $C = 449.53$ Å^6), C–H ($A = 1527$ kJ mol^{-1}, $B = 2.892$ Å^{-1}, $C = 167.51$ Å^6), H–H ($A = 1231$ kJ mol^{-1}, $B = 3.105$ Å^{-1}, $C = 62.42$ Å^6) [40, 41].

The most straightforward method for generating the appropriate intramolecular, molecule–substrate and substrate–substrate potentials is the embedded atom method (EAM) [42], in which each atom is viewed as being embedded in a host lattice consisting of all other atoms. Using this method, we have developed classical many-body EAM potentials for hydrocarbons on Al–Ni–Co alloys by formulating the energy as

$$E = \sum_i F_i(\rho) + \sum_{i\neq j}\phi_{ij}(r).$$

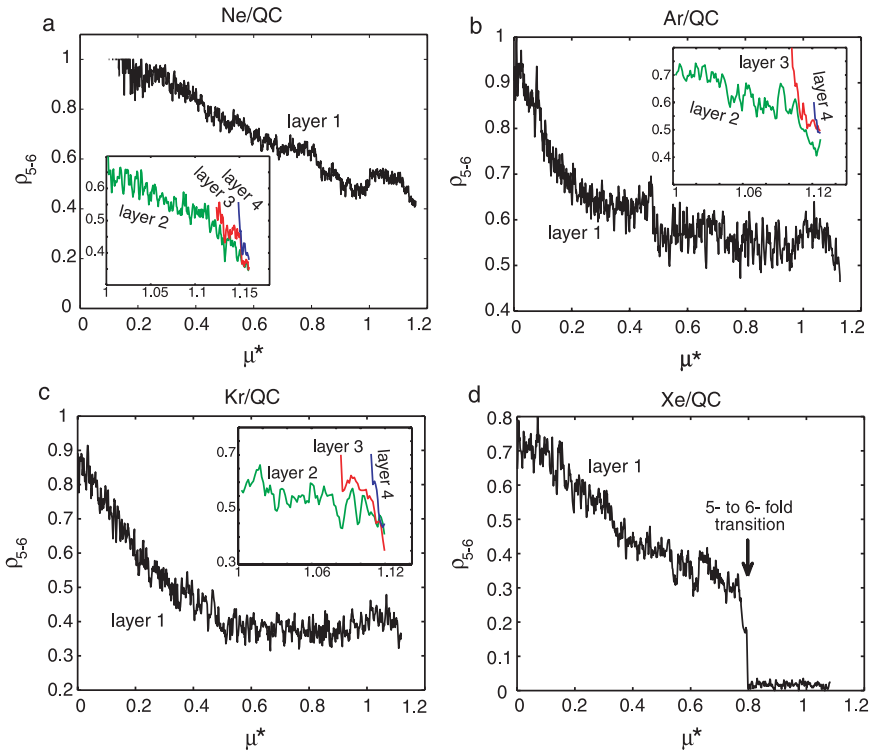

Figure 7. Order parameters ρ_{5-6} as a function of normalized chemical potential μ^* at a reduced temperature $T^* = T/\varepsilon_{gg} = 0.35$, where ε_{gg} is the Lennard-Jones energy parameter for gas–gas interactions, for the first four layers of (a) Ne, (b) Ar, (c) Kr, and (d) for the first layer of Xe. The actual T values are 11.8 K, 41.7 K, 59.6 K, and 77 K, respectively. Figure 5 in [38].

Table 2. Parameter values for the 12-6 Lennard-Jones interactions. TM is the label for Ni or Co. The prefixes i and d refer to hypothetical inflated and deflated variants of real atoms, as discussed in the text. Table 1 in [38].

	ε_{gg} (meV)	σ_{gg} (nm)	ε_{gas-Al} (meV)	σ_{gas-Al} (nm)	ε_{gas-TM} (meV)	σ_{gas-TM} (nm)
Ne	2.92	0.278	9.40	0.264	9.01	0.249
Ar	10.32	0.340	17.67	0.295	16.93	0.280
Kr	14.73	0.360	21.11	0.305	20.23	0.290
Xe	19.04	0.410	24.00	0.330	23.00	0.315
$iNe^{(1)}$	2.92	0.410	5.45	0.330	5.22	0.315
$dXe^{(1)}$	19.04	0.278	41.39	0.264	39.67	0.249
$dXe^{(2)}$	19.04	0.390	25.88	0.320	24.80	0.305
$iXe^{(1)}$	19.04	0.550	14.96	0.400	14.34	0.385
$iXe^{(2)}$	19.04	0.675	10.52	0.462	10.08	0.447

The many-body term, F_i, represents the energy needed to embed the ith atom at a particular position where the total charge density is ρ. The second term is a pair interaction. The total charge density at location i is taken as a sum of atomic charge density from all atoms except the ith atom. In our parameterization of the potentials, we take cubic splines (with 6 or 7 knots) for the embedding functions and the following functionals for the atomic charge density [43] and pair interaction:

$$\rho^{\text{atom}}(r) = \rho_e \exp[-\beta(r/r_e - 1)]$$

$$\phi(r) = D[\exp(-2\alpha(r - r_o)) - 2\exp(-\alpha(r - r_o))]$$

$$\phi_{AB}(r) = \left[\phi_{AA}(r)Z_B/Z_A + \phi_{BB}(r)Z_A/Z_B\right]/2.$$

The last equation is the mixing rule for pair interactions of different types of atom [44].

These parameters are fitted to *ab initio* energies of selected training structures. The training structures are fully relaxed using VASP code and the energy of the relaxed structures is calculated to accuracy better than 10 meV. To get the relaxed structures for the ternary phases of Al–Ni–Co, initial configurations were taken from an alloy database [45]. Among the ternary alloys found there, dB1, dH1, and dH2 are d-Al–Ni–Co approximants. These approximants are known to provide good descriptions of local structures at the ten-fold decagonal Al–Ni–Co surface [22].

The final EAM potentials contain more than 60 fitting parameters. Therefore, the fitting is prone to converge to one of the unphysical local minima. In order to drive the parameters

Table 3. Fitted parameters for EAM potentials for hydrocarbons on Al–Ni–Co. The embedding energy functions are taken as natural cubic splines, with knots expressed in (ρ, F_y), where ρ is in Å^{-3} and F_y is in eV.

	C	H	Al	Co	Ni
ρ_e (Å^{-3})	0.932	1.639	0.026	0.090	0.126
B	5.473	2.798	7.182	5.945	5.447
r_e (Å)	1.240	0.740	2.700	2.280	2.150
D (eV)	0.116	0.224	0.034	0.037	0.039
α (1/Å)	2.786	3.156	1.740	3.636	3.198
r_o (Å)	1.478	1.076	2.938	2.730	2.731
Z/Z_C	1	0.532	0.989	1.115	1.258
Z/Z_H		1	0.857	1.140	0.850
Z/Z_{Al}			1	0.370	0.498
Z/Z_{Co}				1	0.970
knot_1	0, 0	0, 0	0, 0	0, 0	0, 0
knot_2	0.353, −3.860	1.037, −3.475	0.079, −3.038	0.217, −4.216	0.252, −4.354
knot_3	0.519, −5.429	1.527, −3.974	0.108, −3.296	0.358, −6.713	0.327, −4.901
knot_4	0.746, −6.254	1.797, −3.797	0.507, −4.546	0.774, −6.972	0.574, −5.370
knot_5	1.033, −7.443	1.899, −3.744	0.893, −3.903	1.439, −6.665	1.032, −5.752
knot_6	1.824, −7.988	2.200, −3.674	1.408, −3.971	1.635, −6.270	1.354, −5.609
knot_7	2.200, −7.264	—	2.200, −3.141	2.200, −4.639	2.200, −4.574

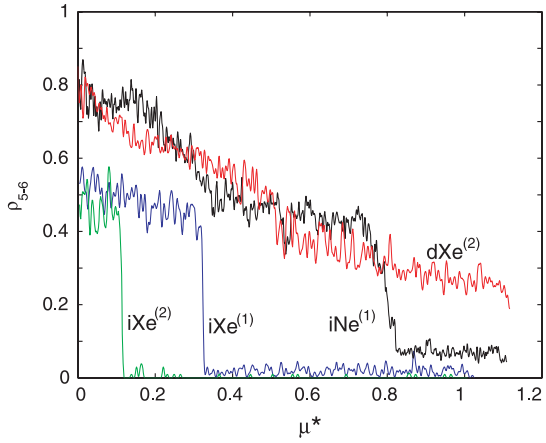

Figure 8. Order parameters as a function of normalized chemical potential for the first layers of $\text{dXe}^{(2)}$, $\text{iNe}^{(1)}$, $\text{iXe}^{(1)}$, and $\text{iXe}^{(2)}$ at $T^* = 0.35$. The first-order five-fold to six-fold transition occurs for all except $\text{dXe}^{(2)}$. Figure 7 in [38].

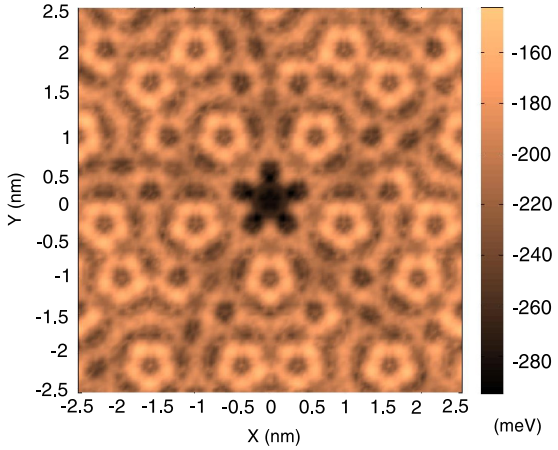

Figure 9. Minimum potential energy surface for methane on a 5.12×5.12 nm^2 section of the Al–Ni–Co quasicrystal. The scale at the right shows the energy scale, which ranges from −320 to −160 meV.

toward a physically meaningful convergence point, the fitting is performed in multiple stages as follows:

(1) fit potentials for elemental Al, Co, and Ni,
(2) fit potentials for d-Al–Ni–Co,
(3) fit potentials for hydrocarbons,
(4) fit final potentials for hydrocarbons on d-Al–Ni–Co.

In stage (1), the elemental potentials for Al, Co, and Ni are fit to elemental bulk energies at different pressures to ensure that the potentials represent stable materials under compression/expansion and yield reasonable lattice constants. In the calculations, the different pressures are achieved by expanding or compressing the relaxed structures, namely at lattice constants from $a = 0.95a_0$ to $a = 1.1a_0$, where a_0 is the equilibrium lattice constant at zero pressure. Training at various pressures increases the transferability of the potentials due to a wider range of charge density covered.

The results from stage (1) are used as initial conditions in stage (2). The potential for systems containing Al, Ni, and Co (AlCoNi-pot) are fit to energies in bulk structures at various lattice constants and to energies in surface configurations. The latter is intended to tune the AlCoNi-pot at low charge density in different non-bulk atomic environments. The surface configurations are created from dH1, dH2, and dB1.

In step (3), the EAM potentials for hydrocarbons (CH-pot) are fitted to energies of isolated structures. The *ab initio* calculations are performed in a fairly large cubic cell with 10 Å vacuum space to minimize the interaction between molecules due to periodic boundary conditions in VASP. The final parameters (step (4)) are fitted to the adsorption energies of various small hydrocarbons on dB1, dH1, and dH2 slabs. The fitted values are summarized in table 3.

Figure 9 shows the calculated methane-quasicrystal potential energy minimum. A comparison to figure 3 indicates

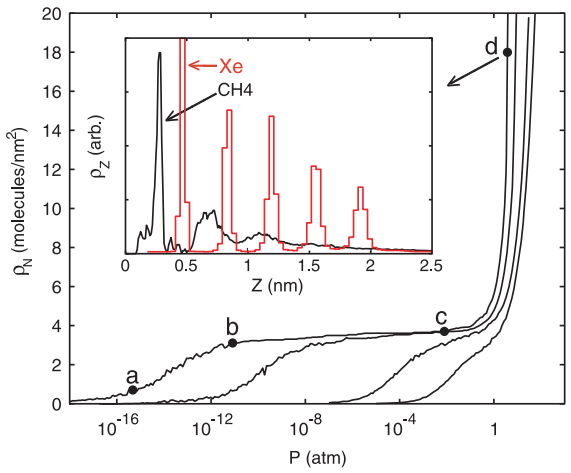

Figure 10. Calculated isotherms for methane on Al–Ni–Co, showing adsorbed density versus P. The T values of the isotherms are chosen to range from $T = 0.75T_t$, where T_t is the 3D triple point temperature of methane, to a temperature just below the critical point temperature of methane. The inset shows the height profile of the adsorbed methane at point d, and for comparison, the same profile for adsorbed Xe.

that this potential looks similar to that for Xe adsorption on this surface (e.g. the locations of lowest potential energy correspond generally to the hollows between substrate atoms) except that the adsorption is slightly stronger. By examining the energies for different methane orientations, we have found that the adsorbed methane molecules are essentially isotropic on this surface. Figure 10 shows the calculated adsorption isotherms for this system. In the temperature range studied here, there is no evidence for dissociation of the methane. Although the adsorption occurs under similar T and P conditions to Xe, the growth is quite different. There are no steps evident in the isotherms that would correspond to the second layer and higher, and the z-profile, shown in the inset, indicates that the layering is not well defined, as it is for Xe.

Figure 11 shows the density plots for methane for two different coverages, corresponding to points 'a' and 'c' on the isotherm in figure 10. The ordering in the first layer is five-fold, also indicated by the Fourier transform, and there is no transition to six-fold for methane, as for Xe. This is shown more clearly in panel 11(d), which shows the order parameter, analogous to those shown in figure 7 for the rare gases. The lack of transition is consistent with our rule based on the rare gases [38] that the size of the rare gas must be at least as large as Xe on this quasicrystal surface for the transition to occur, and the size of methane relative to xenon (ratio of LJ σ parameters) is 0.8 [46]. The height profiles indicate even less layer ordering in the methane than the smaller rare gases, however.

4. Discussion and conclusion

In this paper, we have reviewed our studies of rare gases on the decagonal Al–Ni–Co surface. The adsorption properties of rare gases establish a foundation for understanding the properties of other adsorbed gases. One of the results

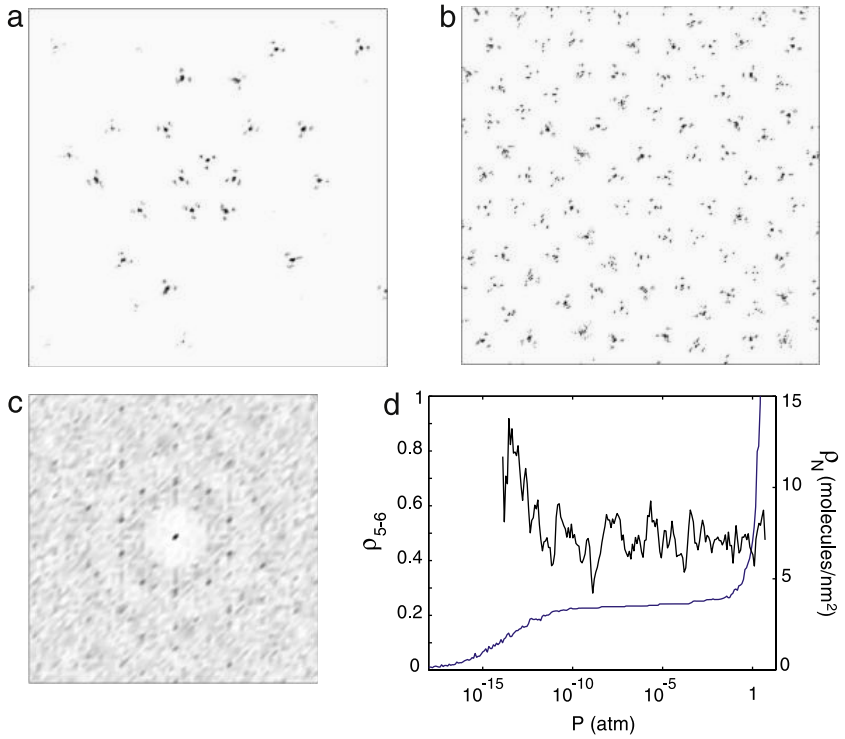

Figure 11. (a) and (b) Calculated density of the methane on the surface at points 'a' and 'c' of the 68 K isotherm shown in figure 10, respectively. (c) Fourier transform of the density plot shown in (b), consistent with five-fold ordering of the methane near monolayer completion. (d) Order parameter (noisy curve, scale on left axis, as calculated for figure 7) as a function of pressure for the $T = 68$ K isotherm (smoother curve, scale on right axis), indicating that there is no sharp transition to six-fold ordering for coverages up to two layers.

obtained from those studies is that the ordering of gases on quasicrystalline substrates depends critically on the relative length scales of the quasicrystalline ordering and the size of the gas molecules. The ordering of gases could be relevant to the use of lubricants with quasicrystalline coatings. In order to address the question of the effect of adsorbed gases on the superlubricity at quasicrystal surfaces, we have developed a method for calculating the adsorption properties of hydrocarbons on quasicrystalline and other alloy surfaces.

The new results for methane adsorption on the quasicrystal surface indicate that although the initial adsorption occurs in a similar temperature range as Xe, the growth of the film is quite different. The methane orders according to the substrate structure in the submonolayer range, and there is no evidence for a transition to six-fold ordering. The lack of steps in the isotherms and the z-profiles indicate that there is little if any layering as the film grows. Thus, for low coverages, methane follows the rule we proposed based on rare gases, that periodic ordering occurs on this quasicrystal when the adsorbed gas molecules are at least as large as Xe. At higher coverages, the film growth is even less ordered than for smaller rare gas atoms, presumably due to the more complex molecular structure. According to our hypothesis expressed in the introduction, because there is no periodic order, a methane film would not be expected to reduce the superlubricity of quasicrystal surfaces. Of course, methane is not a likely lubricant in any real system, and therefore we need to extend these studies to larger hydrocarbons, which are larger than Xe, and according to our rule, might form periodic structures on this surface, affecting the superlubricity.

The computational procedures described here can be extended to larger hydrocarbon molecules, and we have begun this work (not described here) for alkanes as large as octane, and also for different alloy substrates. Clearly, it would be very helpful to have experimental data for these systems, both as a test of the theoretical methods and to test the frictional properties of such films. Our current experimental studies, consisting of temperature-programmed desorption and diffraction studies, will elucidate the former, but will not address the latter, and therefore other experimental studies are desirable.

Acknowledgments

This research was supported by NSF grant DMR-0505160. Acknowledgment is made to the Donors of the American Chemical Society Petroleum Research Fund for partial support of this research. We also acknowledge the Teragrid partnership (TACC Supercomputer Center) for computational resources.

References

[1] Dubois J M 2003 *Useful Quasicrystals* (Singapore: World Scientific)
[2] Hirano M, Shinjo K, Kaneko R and Murata Y 1991 *Phys. Rev. Lett.* **67** 2642
[3] Hirano M, Shinjo K, Kaneko R and Murata Y 1997 *Phys. Rev. Lett.* **78** 1448
[4] Ko J S and Gellman A J 2000 *Langmuir* **16** 8343
[5] Dienwiebel M, Verhoeven G S, Pradeep N, Frenken J W M, Heimberg J A and Zandbergen H W 2004 *Phys. Rev. Lett.* **92** 126101
[6] Dubois J M 1993 *Phys. Scr.* T **49** 17
[7] Park J Y and Thiel P A 2008 *J. Phys.: Condens. Matter* **20** 314012
[8] Park J Y, Ogletree D F, Salmeron M, Jenks C J and Thiel P A 2004 *Tribol. Lett.* **17** 629
[9] Park J Y, Ogletree D F, Salmeron M, Ribeiro R A, Canfield P C, Jenks C J and Thiel P A 2006 *Phys. Rev.* B **74** 024203
[10] Park J Y, Ogletree D F, Salmeron M, Ribeiro R A, Canfield P C, Jenks C J and Thiel P A 2006 *Phil. Mag.* **86** 945
[11] Park J Y, Ogletree D F, Salmeron M, Ribeiro R A, Canfield P C, Jenks C J and Thiel P A 2005 *Science* **309** 1354
[12] Park J Y, Ogletree D F, Salmeron M, Ribeiro R A, Canfield P C, Jenks C J and Thiel P A 2005 *Phys. Rev.* B **71** 144203
[13] Singh A and Tsai A P 2008 *J. Phys.: Condens. Matter* **20** at press
[14] Sharma H R, Shimoda M and Tsai A P 2007 *Adv. Phys.* **56** 403
[15] Franke K J, Gille P, Rieder K-H and Theis W 2007 *Phys. Rev. Lett.* **99** 036103
[16] Fournée V and Thiel P A 2005 *J. Phys. D: Appl. Phys.* **38** R83
[17] Widjaja E J and Marks L D 2003 *Phys. Rev.* B **68** 134211
[18] McGrath R, Ledieu J, Cox E J, Haq S, Diehl R D, Jenks C J, Fisher I, Ross A R and Lograsso T A 2002 *J. Alloys Compounds* **342** 432
[19] Hoeft J T, Ledieu J, Haq S, Lograsso T A, Ross A R and McGrath R 2006 *Phil. Mag.* **86** 869
[20] Ferralis N, Pussi K, Cox E J, Gierer M, Ledieu J, Fisher I R, Jenks C J, Lindroos M, McGrath R and Diehl R D 2004 *Phys. Rev.* B **69** 153404
[21] Cervellino A, Haibach T and Steurer W 2002 *Acta Crytallogr.* B **58** 8
[22] Pussi K, Ferralis N, Mihalkovic M, Widom M, Curtarolo S, Gierer M, Jenks C J, Canfield P, Fisher I R and Diehl R D 2006 *Phys. Rev.* B **73** 184203
[23] Pussi K and Diehl R D 2008 to be published
[24] Krajci M, Hafner J and Mihalkoviç M 2006 *Phys. Rev.* B **73** 134203
[25] Sugiyama K, Nishimura S and Hiraga K 2002 *J. Alloys Compounds* **342** 65
[26] Ferralis N, Diehl R D, Pussi K, Lindroos M, Fisher I R and Jenks C J 2004 *Phys. Rev.* B **69** 075410
[27] Diehl R D, Seyller T, Caragiu M, Leatherman G S, Ferralis N, Pussi K, Kaukasoina P and Lindroos M 2004 *J. Phys.: Condens. Matter* **16** S2839
[28] Trasca R A, Ferralis N, Diehl R D and Cole M W 2004 *J. Phys.: Condens. Matter* **16** S2911
[29] Bruch L W, Diehl R D and Venables J A 2007 *Rev. Mod. Phys.* **79** 1381
[30] Diehl R D, Ledieu J, Ferralis N, Szmodis A W and McGrath R 2003 *J. Phys.: Condens. Matter* **15** R63
[31] Curtarolo S, Setyawan W, Ferralis N, Diehl R D and Cole M W 2005 *Phys. Rev. Lett.* **95** 136104
[32] Diehl R D, Ferralis N, Pussi K, Cole M W, Setyawan W and Curtarolo S 2006 *Phil. Mag.* **86** 863
[33] Setyawan W, Ferralis N, Diehl R D, Cole M W and Curtarolo S 2006 *Phys. Rev.* B **74** 125425
[34] Da Silva J L F, Stampfl C and Scheffler M 2005 *Phys. Rev.* B **72** 075424
[35] Leatherman G S, Diehl R D, Karimi M and Vidali G 1997 *Phys. Rev.* B **56** 6970
[36] Ying S C 1971 *Phys. Rev.* B **3** 4160
[37] Vidali G, Ihm G, Kim H-Y and Cole M W 1991 *Surf. Sci. Rep.* **12** 133

[38] Setyawan W, Diehl R D, Ferralis N, Cole M W and Curtarolo S 2007 *J. Phys.: Condens. Matter* **19** 016007
[39] Diehl R D, Setyawan W, Ferralis N, Trasca R A, Cole M W and Curtarolo S 2007 *Phil. Mag.* **87** 2973
[40] Tsuzuki S, Uchimaru T, Tanabe K and Kuwajima S 1994 *J. Phys. Chem.* **98** 1830
[41] Tsuzuki S, Uchimaru T and Tanabe K 1993 *J. Mol. Struct.* **280** 273
[42] Daw M S and Baskes M I 1983 *Phys. Rev. Lett.* **50** 1285
[43] Herman A 2005 *Int. J. Nanotechnol.* **2** 215
[44] Haftel M I 1993 *Phys. Rev.* B **48** 2611
[45] Widom M and Mihalkoviç M 2007 Alloy database at http://alloy.phys.cmu.edu
[46] Bruch L W, Cole M W and Zaremba E 1997 *Physical Adsorption: Forces and Phenomena* (Oxford: Oxford University Press)
[47] Ancilotto F, Curtarolo S, Toigo F and Cole M W 2001 *Phys. Rev. Lett.* **87** 206103
[48] Curtarolo S, Stan G, Cole M W, Bojan M J and Steele W A 1999 *Phys. Rev.* B **59** 4402